

## Laser-driven ion acceleration using isolated mass-limited spheres

This article has been downloaded from IOPscience. Please scroll down to see the full text article.

2010 New J. Phys. 12 113013

(<http://iopscience.iop.org/1367-2630/12/11/113013>)

View [the table of contents for this issue](#), or go to the [journal homepage](#) for more

Download details:

IP Address: 130.183.90.175

The article was downloaded on 05/01/2011 at 08:37

Please note that [terms and conditions apply](#).

## Laser-driven ion acceleration using isolated mass-limited spheres

T Sokollik<sup>1,5</sup>, T Paasch-Colberg<sup>1,2</sup>, K Gorling<sup>1</sup>, U Eichmann<sup>1</sup>,  
M Schnürer<sup>1</sup>, S Steinke<sup>1</sup>, P V Nickles<sup>1,3</sup>, A Andreev<sup>1,4</sup> and  
W Sandner<sup>1</sup>

<sup>1</sup> Max Born Institute, Max-Born-Straße 2a, D-12489 Berlin, Germany

<sup>2</sup> Max-Planck-Institut für Quantenoptik, Hans-Kopfermann-Straße 1, D-85748 Garching, Germany

<sup>3</sup> Gwangju Institute of Science and Technology, GIST, Gwangju 500-712, Republic of Korea

<sup>4</sup> Vavilov State Optical Institute, St. Petersburg, Russia

E-mail: [Sokollik@mbi-berlin.de](mailto:Sokollik@mbi-berlin.de)

*New Journal of Physics* **12** (2010) 113013 (12pp)

Received 16 May 2010

Published 8 November 2010

Online at <http://www.njp.org/>

doi:10.1088/1367-2630/12/11/113013

**Abstract.** We report on our experiments on laser-driven ion acceleration using fully isolated mass-limited spheres with a diameter down to  $8\ \mu\text{m}$  for the first time. Two-dimensional (2D) particle-in-cell (PIC) and hydro-code simulations were used to show that the pre-plasma at both the front and rear sides of the target strongly affect the efficiency of the ion acceleration. The mechanism of the plasma flow around mass-limited targets has not yet been identified for laser-driven ion acceleration. Our models indicate that this effect is the cause of the observed limitation to the ion-beam energy in both previous experiments and in our own.

### Contents

<b>1. Introduction</b>	<b>2</b>
<b>2. Preparation of mass-limited targets</b>	<b>2</b>
<b>3. Experiments</b>	<b>4</b>
<b>4. Simulation</b>	<b>6</b>
<b>5. Summary</b>	<b>10</b>
<b>Acknowledgments</b>	<b>11</b>
<b>References</b>	<b>11</b>

<sup>5</sup> Author to whom any correspondence should be addressed.

## 1. Introduction

In recent decades, investigation into ion acceleration by intense laser fields has made significant progress, mainly due to advances in both laser technology and in target preparation. Of the laser advances, two of the most important include an increase in the achievable focused laser intensity and an improvement by several orders of magnitude of the temporal pulse contrast. The latter was achieved by the use of sophisticated plasma mirror technology and has allowed the use of extremely thin foils, which in turn has enabled the investigation of novel acceleration mechanisms such as radiation pressure acceleration (RPA) [1]–[4] and several phenomena in the transparent regime [5]–[8], as well as other phenomena such as symmetrical ion emission in the target normal sheath acceleration (TNSA) regime [9]. Meanwhile, mass-limited targets have become the focus of both theoretical [10, 11] and experimental [12, 13] studies, due to expected increases in efficiency and peak ion energy compared to the use of foil targets of similar thickness. Assuming TNSA as the predominant acceleration mechanism, it has been shown in several publications [14, 15] that the electron sheath at the rear side of the target spreads laterally, which decreases the accelerating field. The main idea of using mass-limited targets is to reduce this electron spread by reducing the target surface. In this case, the electrons are confined for a longer time and within a smaller area, thus providing higher accelerating fields.

However, the expected increase in the ion energy has not yet been observed. In fact, the ion energies measured using mass-limited targets in the TNSA regime have been even lower than those achieved with the commonly used extended foils [16]–[19]. We present experiments, particle-in-cell (PIC) simulations and analytical models that explain the mechanisms limiting the ion energies when using mass-limited targets. Fully isolated mass-limited targets of different sizes were used to allow accurate comparison with theoretical results.

## 2. Preparation of mass-limited targets

Two main approaches to prepare isolated mass-limited targets have been pursued so far. The first approach is to mount mass-limited targets on wires [13]. The main challenges here are to produce targets of sufficiently small size (a few microns) and to avoid the influence of mountings on the electron dynamics, which would make the results difficult to compare to theoretical predictions. The latter becomes increasingly difficult to realize as the target size becomes smaller. This technology is not suited for experiments at higher repetition rate.

The second approach, which circumvents the problem of mechanical mounting, is based on liquid jet technology [16]–[19]. Water micro-droplets can be generated regularly spaced in a freely moving chain. The droplet diameters are in the range of 15–20  $\mu\text{m}$ . The targets can be used at a high repetition rate limited only by the repetition rate of available laser systems. In experiments using these targets, mono-energetic proton spectra have been observed under special circumstances [16]. However, the maximum proton energy of about 1 MeV observed from water droplets is relatively low compared to energies obtained using foils. Using foils of a similar thickness, energies above 3 MeV were observed with the same laser parameters [20]. Using proton imaging, we recently found that the influence of adjacent droplets, as well as the surrounding gas, cannot be neglected [12, 21].

In the present experiments, we realized a novel approach for investigating the physical mechanism of laser-driven ion acceleration from mass-limited targets. To prepare fully isolated

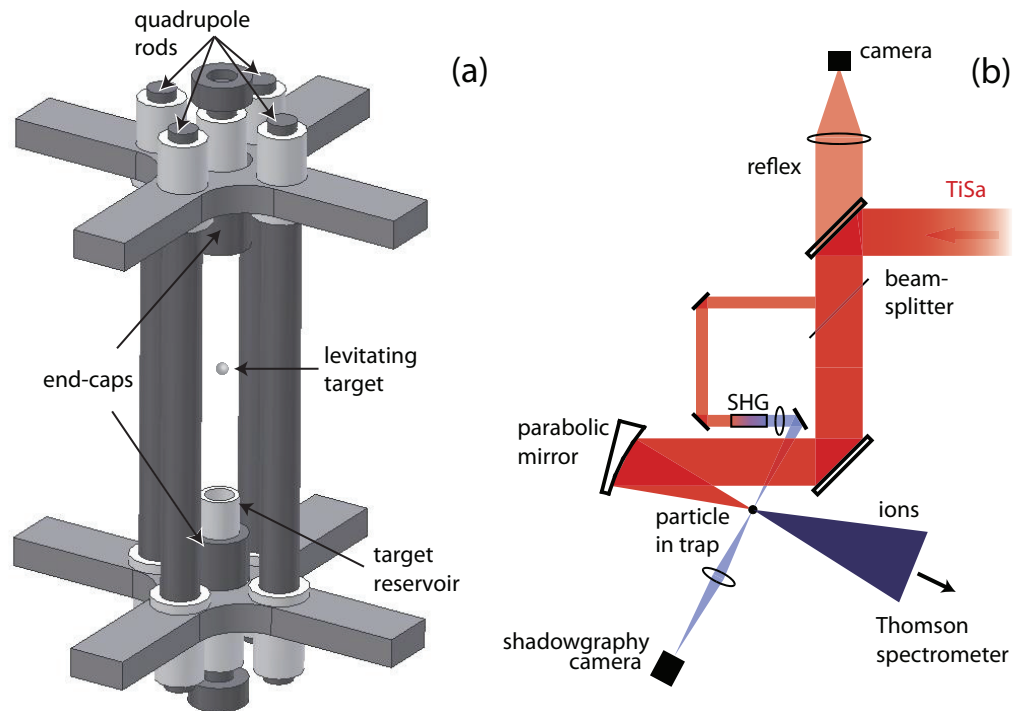


**Figure 1.** (a) Linear Paul trap used in the experiments. Besides the four trap rods, it consists of two end-caps and a target supply attached to the lower end-cap. (b) Experimental setup, the laser is focused on the levitated spheres using an  $f/2.5$  off-axis parabolic mirror. A small fraction of the laser pulse energy ( $\sim 4\%$ ) is split from the main beam and frequency doubled in a BBO crystal for shadowgraphy measurements.

targets, without the influence of mountings, neighboring targets or ambient plasma, we set up a linear Paul trap [22]–[24] (figure 1(a)). The trap consists of four symmetrically arranged rods (electric quadrupole) made of stainless steel of 40 mm length and a diameter of 4 mm. The rods are separated by 6 mm from surface to surface. This spacing is wide enough to allow for laser beam access, optical diagnostics and extraction of accelerated charged particles and analysis of them in a Thomson spectrometer. Radial trapping is achieved by applying alternating high voltages at a frequency of about 400 Hz with typically 4 kV peak-to-peak square wave voltage to paired opposite rods with opposite amplitude, respectively. Two cylindrical end-caps of 6 mm diameter and separated by 3 cm are located on the trap axis, where static voltages can be applied to confine the target motion axially. Furthermore, the lower end-cap is machined to serve both as an end-cap and as a reservoir of target spheres. The trap is oriented parallel to the Earth’s gravitational field. Thus, axial confinement is achieved by applying a static voltage to the lower end-cap alone to hold the trapped particle against gravity. The upper end-cap is mainly used for particle manipulation or active cooling in the axial direction. We are able to trap spheres made of glass or plastic with diameters of 5–30  $\mu\text{m}$  and lycophyte spores of similar sizes.

Residual micro-motion as well as vibrations of the vacuum chamber limit the achievable spatial confinement of the spheres. The residual positional variation was measured by a shadowgraphy technique (cf figure 1(b)) to be 2.14  $\mu\text{m}$  (standard deviation) in the horizontal direction and 6.18  $\mu\text{m}$  (standard deviation) in the vertical direction.

### 3. Experiments

The experiments were performed with the multi-TW Ti:Sa laser at the Max-Born-Institute that has a pulse duration of 45 fs and a pulse energy of about 1.2 J. The temporal shape of the laser pre-pulse has been measured with a fast photodiode and a third-order autocorrelator. Using linear functions, the temporal evolution of the pulse can be described as follows: from  $-1000$  to  $-7.8$  ps the relative intensity grows from 0 to  $3.5 \times 10^{-8}$ , from  $-7.8$  to  $-1.4$  ps the relative intensity grows from  $3.5 \times 10^{-8}$  to  $4 \times 10^{-7}$  and from  $-1.4$  and 0 ps the intensity grows up to the main peak at 0 ps. Focusing under  $f/2.5$  conditions and measuring the energy content in a  $5 \mu\text{m}$  in diameter focal spot gives an intensity of about  $3 \times 10^{19} \text{ W cm}^{-2}$ . The laser beam pointing stability gives rise to a laser focus fluctuation with a standard deviation of about  $\pm 1 \mu\text{m}$  in the plane transversal to the beam propagation. Including the movement of the target spheres, we estimate a probability of about 22% to hit a sphere with a diameter of  $10 \mu\text{m}$ . Since the probability for the laser to hit a sphere decreases with its diameter, only spheres larger than  $8 \mu\text{m}$ , for which a significant number of spectra were recorded, are considered in this paper. We observed four different kinds of ion spectra in the experiments: (i) narrow energy bandwidth spectra of protons and heavy ions, (ii) proton spectra with dips, (iii) broad energy spectra and (iv) spectra of heavy ions only. The occurrence of this feature is varying from shot to shot and is in all probability correlated with the position of the laser–sphere interaction (central/non-central hit).

In figure 2, proton spectra with narrow energy bandwidths are shown. The occurrence of this feature is in all probability correlated with a central irradiation of the sphere (in contrast to a non-central hit). Similar results, but with a much lower appearance, were observed in [16] where water and heavy water droplets were used. A multispecies model accounts for both experiments and explains the formation of the quasi-monoenergetic ion beam [25]. The variations in the position and width of the quasi-monoenergetic feature in figure 2 could be due to fluctuations of the temporal contrast [25] and of the laser energy. Also, the thickness of the contamination layer differs from sphere to sphere, which influences the position of the peak. The interplay between the light ion species (proton) and the heavy ion species (oxygen in the case of water, and silicon and/or oxygen in the case of glass) plays an essential role. Nevertheless, there is an important difference: in the case of the glass spheres, protons can only originate from a contamination layer of several nanometer thickness in contrast to water droplets, where a proton-rich layer is always available and cannot be ablated or suppressed.

Using glass-sphere targets, we observe proton spectra with a broad continuous thermal distribution (figure 3(b)), as well as spectra with dips (figure 3(a)) up to the situation where only the heavy ion species were present. We attribute this observation to the fact that the contamination layer can be quite different. Glass spheres are produced and then packed under vacuum-sealed conditions. In our experiments, we open the sealing and put some amount of glass-sphere powder to the injector of the trap. We thus have a mixture of spheres that have been exposed to usual atmospheric conditions in quite a different way, simply by their position (at the surface or inside the glass-sphere powder sample). Therefore, the number of available protons is crucial for the experimental outcome. In the case of a lower number, the probability of formation of quasi-monoenergetic spectra is enhanced as is discussed in several works [26]–[29] and generally described with the ‘test particle in field’ approach. In figure 2(a), we include a 2D-PIC simulation. In the simulation, the following parameters have been used: a sphere of  $10 \mu\text{m}$  diameter, a laser intensity of  $I_L = 3 \times 10^{19} \text{ W cm}^{-2}$ , a pulse duration of 45 fs and a focus

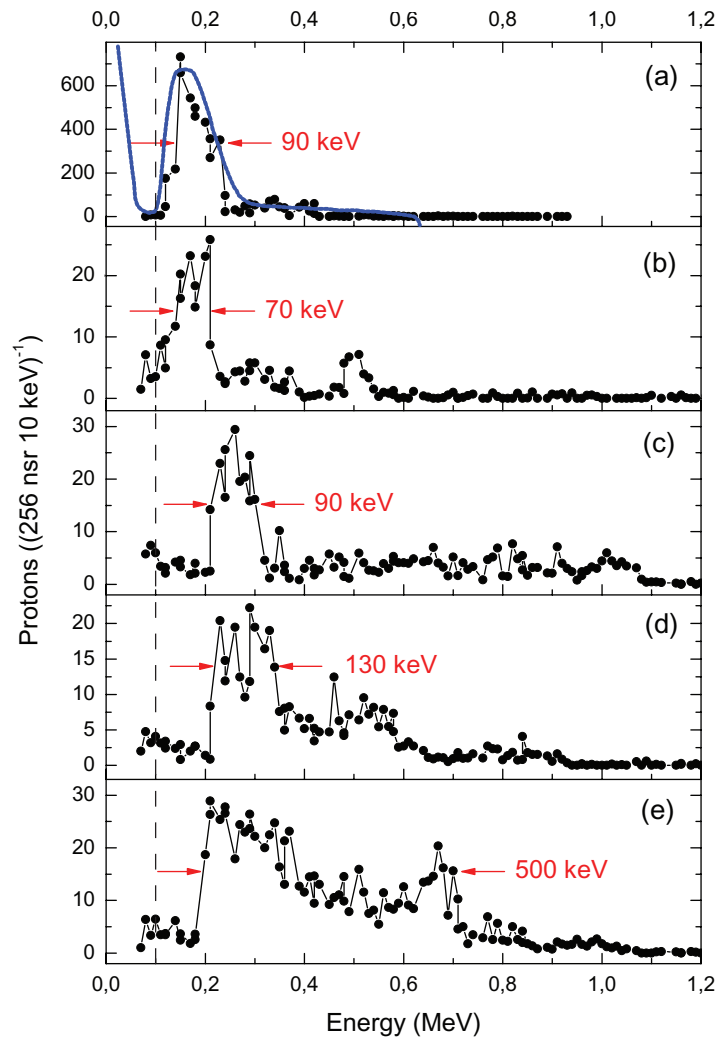


**Figure 2.** Recorded proton spectra from glass spheres with  $11 \pm 1 \mu\text{m}$  diameter. All spectra show quasi-monoenergetic features with different bandwidths and central energies. The blue line in (a) represents the results from a two-dimensional (2D) PIC simulation. The dashed line represents the lower detection limit of the spectrometer caused by the edge of the detector.

diameter of  $5 \mu\text{m}$ . The crucial parameters for the peak formation in terms of energy and width are the number of protons and their density distribution at the interface. Different simulations have shown that this distribution, which is characterized by the plasma gradient, influences the ion energy very sensitively. This parameter is mainly responsible for the lowering of ion energies in comparison to the expected values at the given laser intensity. The following discussion is devoted to this aspect.

In previous experiments using mass-limited targets in the TNSA regime, cut-off energies comparable to foils have never been obtained [16]–[19]. In the present experiments, one can exclude any influence of surrounding plasma or even adjacent objects as observed for the water droplets [12]. Thus, it is conclusive that the limitation of the proton energy has its origin in the

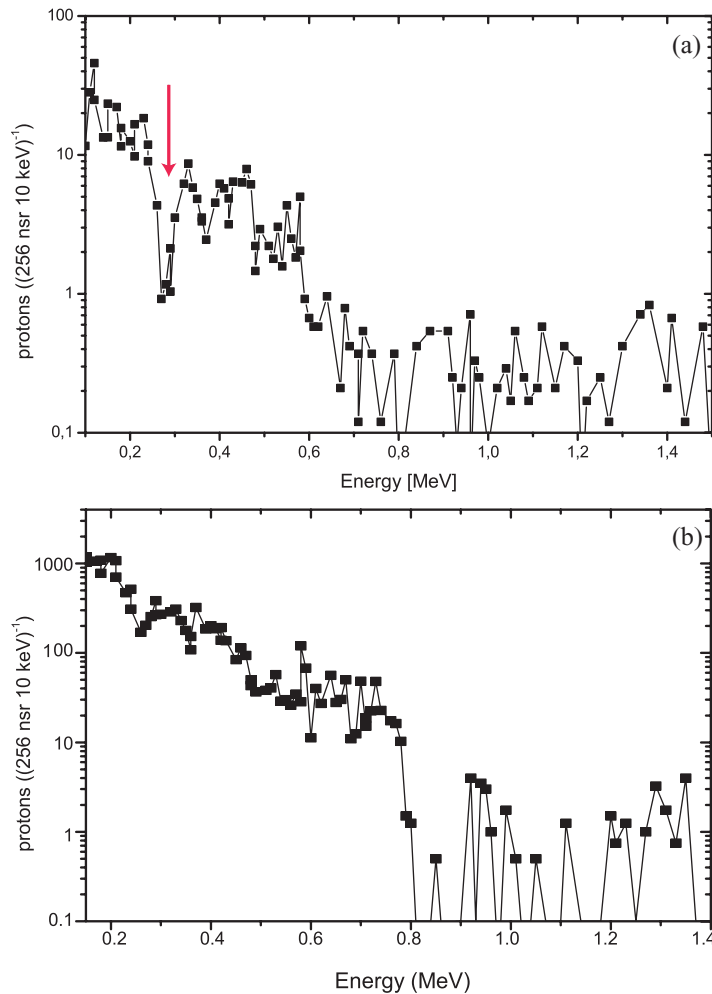


**Figure 3.** (a) Proton spectra with dip at around 0.3 MeV. (b) Continuous proton spectra with a cut-off at around 0.75 MeV. In both the cases, glass spheres with a diameter at around  $12 \mu\text{m}$  were used.

geometry of the target or is due to its mass limitation. In several publications, the influence of the plasma density gradient at the plasma–vacuum interface was investigated [30, 31]. The final proton energy strongly depends on the density gradient and its profile. Some analytical model approaches predict a functional dependence of a plasma temperature and maximum attainable ion energies for a TNSA process [20, 26]. These models give a qualitative guide but cannot reproduce our data in a satisfactory way. In the following section, we present a more detailed simulation.

#### 4. Simulation

We simulate the interaction of a laser pre-pulse, mainly caused by amplified spontaneous emission (ASE) with a sphere using a 2D hydro-code [32], assuming a pre-pulse with a duration of  $\tau_p = 0.5 \text{ ns}$  and an intensity of  $I_p = 1 \times 10^{12} \text{ W cm}^{-2}$ . This approximation of the pre-pulse compared to the more complex shape described in the experimental section simplifies the analytical terms and results in only a slight underestimation of the pre-pulse in the simulation

results (e.g. a 25% smaller  $L_b$ , see the following paragraphs). The sphere was modeled as an infinite cylinder in the 2D simulation [33]. The system of hydrodynamic equations is solved using Euler variables. The energy transport by radiation is described using the three-temperature approximation [34]. The degree of ionization of the plasma is defined as a function of density and temperature. This dependence was obtained as a result of quantum-mechanical calculations and is used in the form of tables and approximation formulae constructed on the basis of them [35]. The code delivers a density profile, which can be approximated by an exponential function at the irradiated target front with a sub-micron scale length of  $L_f$  for a sphere with a diameter of about  $10 \mu\text{m}$ . Then a 2D PIC code is used to compute the ion energies.

The laser parameters used in the simulation are matched to the experimental values. In the simulation, we use a cylinder with a diameter ( $d$ ) between 5 and  $30 \mu\text{m}$  of  $\text{O}^{5+}$  to model the glass sphere. The ion density was set to  $3 \times 10^{22} \text{cm}^{-3}$  and a thin (of the order of 10 nm) surface layer of  $\text{H}^+$  with an areal density of  $3 \times 10^{16} \text{cm}^{-2}$  is used for the model calculations of a rectangular density profile. The plasma density gradient that depends on the pre-pulse parameter as well as the shape of the target influences the absorption coefficient [26]. The simulations show a significant increase of the absorption coefficient and the electron temperature for an increasing scale length of the front side plasma.

In the case of a mass-limited target, the limited size enables electrons born at the front side to reach the rear side. These low energetic electrons are trapped by the space charge close to the target surface and diffuse laterally. They distribute along the target surface and heat the surface layer, which transforms into a coronal plasma layer around the target. Thus, a density gradient ( $L_b$ ) at the rear side of the target is created, which decreases the acceleration fields and limits the achievable proton energies. Within the duration of the pre-pulse  $\tau_p$  the lateral extension of the plasma layer is calculated on the basis of a thermal diffusion process. The characteristic diffusion length of the thermal electron propagation can be estimated by  $l_d = \sqrt{v_{T_e} \tau_p l_e}$ , where  $T_e$  is the electron temperature,  $v_{T_e} = \sqrt{T_e/m_e}$ , and  $l_e$  is the electron free path in a plasma generated by the laser pre-pulse. For our pre-pulse parameters and a sphere diameter of  $d = 10 \mu\text{m}$  the calculated electron temperature is about  $T_e \cong \eta_p I_p \tau_p / n_{e0} d \approx 30 \text{eV}$ , where  $\eta_p \approx 1$  is the absorption coefficient and  $n_{e0} \approx 10^{23} \text{cm}^{-3}$  is the initial electron density. The estimated diffusion length in an oxygen surface plasma with critical plasma density is  $l_d \approx 20 \mu\text{m}$ , and is  $l_d \approx 4 \mu\text{m}$  for solid density.

If the diffusion length  $l_d$  is larger than the target extension  $l_{u/2} = \pi d/2$ , a plasma density gradient  $L_b$  forms at the target rear side, which strongly affects the ion acceleration mechanism. The plasma scale length at the rear side depends on the time and distance the electrons need to propagate to the rear side. The maximal ion energy for a given pre-pulse parameter has a local maximum when the extension of the target equals the diffusion length  $l_{u/2} \approx l_d$ . For our pre-pulse parameter, the highest ion energies are predicted for spheres with a diameter of about  $13 \mu\text{m}$ . Larger target size reduces the effect of the mass-limited targets—the confinement of the electrons. Smaller target size causes a rear side plasma. Both phenomena decrease the proton energy.

In [13], mounted plastic spheres with a diameter of  $15 \mu\text{m}$  were used as mass-limited targets. The relatively high proton energies of 8 MeV observed in this experiment are attributed by the authors to laser-driven shock acceleration, in which case the rear side plasma gradient has a negligible influence on the ion energies. Thus, these results are not in contradiction to our model. Since the laser intensities used in the present experiments are much lower, TNSA is the dominant acceleration process. In figure 4, the experimental and calculated maximal proton energies for spheres of different diameters are shown.

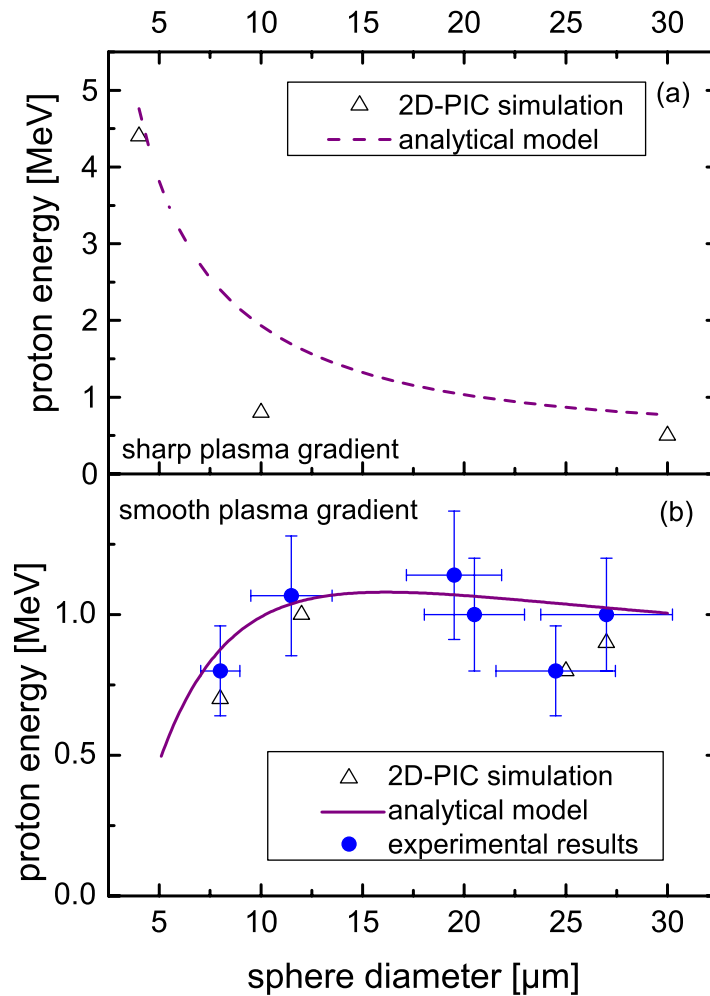


**Figure 4.** (a) The triangles are the calculated maximal proton energies dependent on target size  $d$  for spherical targets with a sharp plasma gradient  $L_f = L_b = 0$  (2D-PIC code). The dashed line shows the analytical model (equation (1)). (b) The triangles are the calculated maximal proton energies for spherical targets with diameters of  $d = 8, 12, 25$  and  $27.5 \mu\text{m}$  and with the corresponding plasma scale lengths of  $L_b = 0.3, 0.15, 0$  and  $0 \mu\text{m}$ . The solid line shows the analytical model for a smooth plasma gradient  $L_0 \approx 10 \mu\text{m}$ . Blue dots represents the maximal proton energies observed in the experiments using glass spheres ( $8\text{--}12 \mu\text{m}$ ) and lycophyte spores ( $19\text{--}27 \mu\text{m}$ ).

Simulations of the electron distribution function using a target with a large diameter and rectangular density profiles have shown a significant cooling of hot electrons, especially after the laser pulse interaction. The maximal energy and temperature of the hot electrons drop by approximately a factor of two within a time interval of 3 times the laser pulse duration. Such cooling is connected with an increase of the hot electron volume caused by the propagation of the hot electrons through the target and around its surface. Since the cooling occurs at a shorter time scale compared to the ion acceleration, a part of the electron energy is lost for the acceleration process.

The degradation of the interface at the rear side leads to reduced proton energies, as shown in figure 4. With further decrease of the sphere size to  $4 \mu\text{m}$  (which is approximately the laser spot size), the maximal proton energy increases if a sharp density profile is present. Here, the effect of electron acceleration on the target surface by the laser fields [36] is dominant. In a spherical target, the electrons have chances of propagating around the target [11] and interacting again with the laser pulse before its end. The fast electron expansion velocity around the target surface is  $v_{\text{es}} \approx 0.5c$ . Thus, it takes the electrons  $\pi d/2v_{\text{es}} \approx 40 \text{ fs}$  ( $d = 4 \mu\text{m}$ ) to be reinserted to the interaction zone. Through repeated interactions of the fast electrons with the laser pulses they gain energy proportional to the number of passages they make through the target front side [37].

The maximal ion energy can be estimated analytically by the following formula [26]:

$$\varepsilon_{\text{im}}(d) \approx 2^{\beta/2} \varepsilon_{\text{ch}}(d) \ln^{\beta} \left( \frac{1 + \sqrt{2e_0 + L_b(d)/r_{\text{Dh}}(d)}}{\sqrt{2e_0 + L_b(d)/r_{\text{Dh}}(d)}} \right), \quad (1)$$

where  $e_0 = 2.7183 \dots$  and  $r_{\text{Dh}} = \sqrt{\varepsilon_{\text{ch}}\varepsilon_0/e^2n_{\text{ch}}(d)}$  is the Debye radius with the vacuum permittivity  $\varepsilon_0$ .  $\varepsilon_{\text{ch}}$  is the average energy and  $n_{\text{ch}}$  the density of fast electrons. The parameter  $1 \leq \beta \leq 2$  describes the different regimes of ion acceleration, where  $\beta = 1$  corresponds to the adiabatic regime and  $\beta = 2$  corresponds to the isothermal one. Since the regime of acceleration is changing dependent on the target size, we used the average  $\beta = 1.5$ , which describes our interval of target diameters ( $4\text{--}30 \mu\text{m}$ ) reasonably. For small targets  $d < l_d$ , the front side gradient is equal to the rear side gradient  $L_f = L_b$ . The front and rear side gradients are obtained from Hydro-code simulations and can be approximated by  $L_f(d) = L_0(d/d_L - 0.8)/(d/d_L + 3)$  and  $L_b(d) = 0.2L_0/(1 + d/d_L)^2$ , respectively, where  $d_L$  is the laser spot size,  $L_0 \approx \tau_p \sqrt{2T_e/m_i}$ , and  $m_i$  is the ion mass.

The dependence of the fast electron energy on the target size can be derived from two energy limits: the energy of an unlimited target,  $\varepsilon_{\text{ch}}^{\infty} = m_e c^2 (\sqrt{1 + 0.7\lambda_{\mu\text{m}}^2 I_{18}} - 1)$ , and the electron energy of a target with the size of the laser spot diameter ( $d_L$ ),  $\varepsilon_{\text{ch}}^{(0)} \approx \eta I/n_{\text{ch}0}c$ , where  $\eta \approx 0.07 + (0.1 + 0.06L_f/\lambda_L)I_{18}/(15 + I_{18})^{0.8}$  is the absorption coefficient at  $d > d_L$  and  $I_{18}$  is the laser intensity in units of  $10^{18} \text{ W cm}^{-2}$  [38, 39].

The electron cooling caused by expansion is taken into account by the adiabatic law:  $\varepsilon_{\text{ch}}(d)V^{\gamma-1} \approx \text{const}$ , where  $V$  is the electron volume,  $\gamma = 2$  for surface expansion and  $\gamma = 5/3$  for volume expansion. This leads to a dependency of the electron energy on the target size  $\varepsilon_{\text{ch}} = \varepsilon_{\text{ch}}(d)$ . Using  $n_{\text{ch}}(d) = n_{\text{ch}0}(d_L/d)^{\alpha}$ , where  $\alpha \leq 1$  (for surface expansion) depends on the expansion regime, one can get  $\varepsilon_{\text{ch}}(d) = \varepsilon_{\text{ch}}^{(0)}(d_L/d)^{\alpha(\gamma-1)}$  for small target sizes. The power  $\alpha$  and the initial fast electron density  $n_{\text{ch}0}$  depend on the plasma gradient. We stress that an ‘unlimited’ target means that  $d$  exceeds some characteristic diameter of the hot electron spot [40]  $d_{\text{max}} = 100 \mu\text{m}$  (in our conditions). The transition from one to the other limit can be described by the following interpolation formula:

$$\varepsilon_{\text{ch}}(d) \approx \varepsilon_{\text{ch}}^{(0)} \left( \frac{d_L}{d} \right)^{\alpha(\gamma-1)} + \varepsilon_{\text{ch}}^{(\infty)} \left( \frac{d - d_L}{d_{\text{max}} - d_L} \right)^{\alpha(\gamma-1)}. \quad (2)$$

Thus, there are two contradictory tendencies which influence the ion energy. One can gain higher ion energies by increasing the plasma scale length at the front side and decreasing the target size. On the other hand, increasing the plasma scale length at the rear side decreases the

ion energy. However, if the plasma scale length at the rear side  $L_b$  is significantly smaller than the Debye radius  $r_{Dh}$  its influence on the acceleration fields can be neglected. Thus, with the condition  $L_b \approx 0.1r_{Dh}$ , one can roughly estimate the required contrast ( $I_p/I_L \approx 4.8 \times 10^{-9}$ ) for an undisturbed rear side for our parameters ( $I_L = 3 \times 10^{19} \text{ W cm}^{-2}$ ,  $r_{Dh} \approx 0.9 \mu\text{m}$ ,  $\tau_p = 0.5 \text{ ns}$ ,  $d = 10 \mu\text{m}$ ).

As a result, the dependence of the ion energy on the target size shows a weak local maximum. In figures 4(a) and (b), the experimental data and theoretical results are shown. The model calculations are visualized by dashed and solid lines. The solid line in figure 4(b) depicts results that have been obtained for a smooth plasma gradient with  $L_0 \approx 10 \mu\text{m}$ ,  $\gamma = 2$ ,  $\alpha = 0.5$ ,  $n_{eh0} = 7 \times 10^{20} \text{ cm}^{-3}$ , and the dashed line in figure 4(a) represents a sharp plasma gradient with  $L_0 = 0$ ,  $\gamma = 2$ ,  $\alpha = 1$  and  $n_{eh0} = 1.25 \times 10^{20} \text{ cm}^{-3}$ . The triangles in figure 4(a) are the results of a PIC simulation for a rectangular plasma density profile and the triangles in figure 4(b) are the PIC simulation data for different diameters and their corresponding plasma density gradients. The dots represent the experimental data. It is visible that our model, which takes growth of electron temperature for decreasing target size into account, qualitatively reproduces the simulation results. The results were also compared to a 3D PIC simulation. For a  $10 \mu\text{m}$  sphere, the obtained maximal proton energy was only 30% higher.

In addition, simulations of mass-limited foils with a size between 8 and  $100 \mu\text{m}$  and a thickness between 2 and  $30 \mu\text{m}$  have been performed. For a rectangular plasma density profile (ultrahigh contrast) the maximal proton energy was slightly lower (30%) compared to similar cylinder targets with the same thickness. Introducing a smooth plasma density profile significantly decreases the maximal proton energy, especially for a small planar target in the same manner as for cylindrical ones. A detailed discussion of these results will be published elsewhere.

In figure 4, the difference between a plasma with a sharp gradient and a plasma with a smooth plasma gradient is clearly visible. The experimental data are reproduced using different scale lengths depending on the target size and remain relatively constant at about 1 MeV. However, the model and PIC simulations assuming a sharp density profile predict a stronger dependence on the target size and an increase of the proton energy to almost 5 MeV for a  $4 \mu\text{m}$  sphere. These energies are comparable to results achieved with similar lasers and extended planar target types [41].

## 5. Summary

In summary, we have investigated laser-driven ion acceleration from fully isolated, mass-limited spherical targets. We were able to use isolated single spheres with a diameter down to  $8 \mu\text{m}$  to exclude any influencing or perturbing objects close to the target. The 2D-PIC and Hydrocode simulations are in good agreement with the experimental results. Our model explains the relatively low ion energy observed in the present experiments as well as in previous experiments using spherical mass-limited targets. The ion energy of mass-limited targets decreases if the electrons created by the pre-pulse are able to reach the rear side of the target before the acceleration fields are generated. Thus mass-limited targets are more sensitive to the temporal contrast of the laser pulse and an ultrahigh contrast is required for overcoming this limitation mechanism. Furthermore, relatively large spherical targets show a faster electron cooling, which leads to a reduction of ion energy. Simulations show that this tendency will change if the diameter of the spheres is comparable to the laser focus.

## Acknowledgments

This work was partially supported by DFG–Sonderforschungsbereich Transregio TR18, GRK 1203 and an EU grant (Marie Curie; no. PIFI-GA-2008-221727).

## References

- [1] Henig A *et al* 2009 Radiation-pressure acceleration of ion beams driven by circularly polarized laser pulses *Phys. Rev. Lett.* **103** 245003
- [2] Robinson A P L, Zepf M, Kar S, Evans R G and Bellei C 2008 Radiation pressure acceleration of thin foils with circularly polarized laser pulses *New J. Phys.* **10** 013021
- [3] Liseykina T V, Borghesi M, Macchi A and Tuveri S 2008 Radiation pressure acceleration by ultraintense laser pulses *Plasma Phys. Control. Fusion* **50** 124033
- [4] Macchi A, Veghini S, Liseykina T V and Pegoraro F 2010 Radiation pressure acceleration of ultrathin foils *New J. Phys.* **12** 045013
- [5] Yin L, Albright B J, Hegelich B M and Fernandez J C 2006 GeV laser ion acceleration from ultrathin targets: the laser break-out afterburner *Laser Part. Beams* **24** 291
- [6] Steinke S *et al* 2010 Efficient ion acceleration by collective laser-driven electron dynamics with ultra-thin foil targets *Laser Part. Beams* **28** 215–21
- [7] Henig A *et al* 2009 Enhanced laser-driven ion acceleration in the relativistic transparency regime *Phys. Rev. Lett.* **103** 045002
- [8] Andreev A A, Steinke S, Sokollik T, Schnurer M, Ter Avetsiyan S, Platonov K Yu and Nickles P V 2009 Optimal ion acceleration from ultrathin foils irradiated by a profiled laser pulse of relativistic intensity *Phys. Plasmas* **16** 013103
- [9] Ceccotti T, Lévy A, Popescu H, Réau F, D’Oliveira P, Monot P, Geindre J P, Lefebvre E and Martin Ph 2007 Proton acceleration with high-intensity ultrahigh-contrast laser pulses *Phys. Rev. Lett.* **99** 185002
- [10] Psikal J, Limpouch J, Kawata S and Andreev A A 2006 Pic simulations of femtosecond interactions with mass-limited targets *Czech. J. Phys.* **56** B515–21
- [11] Limpouch J, Psikal J, Andreev A A, Platonov K Y and Kawata S 2008 Enhanced laser ion acceleration from mass-limited targets *Laser Part. Beams* **26** 225–34
- [12] Sokollik T, Schnurer M, Steinke S, Nickles P V, Sandner W, Amin M, Toncian T, Willi O and Andreev A A 2009 Directional laser-driven ion acceleration from microspheres *Phys. Rev. Lett.* **103** 135003
- [13] Henig A *et al* 2009 Laser-driven shock acceleration of ion beams from spherical mass-limited targets *Phys. Rev. Lett.* **102** 095002
- [14] McKenna P *et al* 2007 Lateral electron transport in high-intensity laser-irradiated foils diagnosed by ion emission *Phys. Rev. Lett.* **98** 145001
- [15] Sokollik T *et al* 2008 Transient electric fields in laser plasmas observed by proton streak deflectometry *Appl. Phys. Lett.* **92** 091503
- [16] Ter-Avetisyan S, Schnurer M, Nickles P V, Kalashnikov M, Risse E, Sokollik T, Sandner W, Andreev A and Tikhonchuk V 2006 Quasimonoegetic deuteron bursts produced by ultraintense laser pulses *Phys. Rev. Lett.* **96** 145006
- [17] Kemp A J and Ruhl H 2005 Multispecies ion acceleration off laser-irradiated water droplets *Phys. Plasmas* **12** 033105
- [18] Schnurer M, Ter-Avetisyan S, Busch S, Risse E, Kalachnikov M P, Sandner W and Nickles P 2005 Ion acceleration with ultrafast laser driven water droplets *Laser Part. Beams* **23** 337–43
- [19] Karsch S, Düsterer S, Schwoerer H, Ewald F, Habs D, Hegelich M, Pretzler G, Pukhov A, Witte K and Sauerbrey R 2003 High-intensity laser induced ion acceleration from heavy-water droplets *Phys. Rev. Lett.* **91** 015001

- [20] Schnurer M, Ter-Avetisyan S, Nickles P V and Andreev A A 2007 Influence of target system on the charge state, number, and spectral shape of ion beams accelerated by femtosecond high-intensity laser pulses *Phys. Plasmas* **14** 033101
- [21] Sokollik T, Schnurer M, Ter-Avetisyan S, Steinke S, Nickles P V, Sandner W, Amin M, Toncian T, Willi O and Andreev A A 2009 Proton imaging of laser irradiated foils and mass-limited targets *Laser-Driven Relativistic Plasmas Applied to Science, Industry and Medicine: 2nd Int. Symp.* vol 1153 pp 364–73
- [22] Ghosh P 1995 *Ion Traps* (Oxford: Clarendon)
- [23] Raizen M G, Gilligan J M, Bergquist J C, Itano W M and Wineland D J 1992 Ionic crystals in a linear Paul trap *Phys. Rev. A* **45** 6493
- [24] Kwapien T, Eichmann U and Sandner W 2007 Sympathetic cooling of laser-produced doubly charged ions in a few-ion crystal *Phys. Rev. A* **75** 063418
- [25] Brantov A V, Tikhonchuk V T, Klimo O, Romanov D V, Ter-Avetisyan S, Schnurer M, Sokollik T and Nickles P V 2006 Quasi-mono-energetic ion acceleration from a homogeneous composite target by an intense laser pulse *Phys. Plasmas* **13** 122705
- [26] Andreev A A, Kawata S and Platonov K Yu 2006 Effect of a laser prepulse on fast ion generation in the interaction of ultra-short intense laser pulses with a limited-mass foil target *Plasma Phys. Control. Fusion* **48** 1605
- [27] Robinson A P L, Bell A R and Kingham R J 2006 Effect of target composition on proton energy spectra in ultraintense laser-solid interactions *Phys. Rev. Lett.* **96** 035005
- [28] Murakami M and Basko M M 2006 Self-similar expansion of finite-size non-quasi-neutral plasmas into vacuum: relation to the problem of ion acceleration *Phys. Plasmas* **13** 012105
- [29] Tikhonchuk V T, Andreev A A, Bochkarev S G and Bychenkov V Y 2005 Ion acceleration in short-laser-pulse interaction with solid foils *Plasma Phys. Control. Fusion* **47** B869–77
- [30] Kaluza M, Schreiber J, Santala M I K, Tsakiris G D, Eidmann K, Meyer-ter Vehn J and Witte K J 2004 Influence of the laser prepulse on proton acceleration in thin-foil experiments *Phys. Rev. Lett.* **93** 045003
- [31] Grismayer T and Mora P 2006 Influence of a finite initial ion density gradient on plasma expansion into a vacuum *Phys. Plasmas* **13** 032103
- [32] Andreev A A and Kurnin I V 1996 Numerical simulation of subpicosecond laser plasma x-ray emission *J. Opt. Soc. Am. B* **13** 402–5
- [33] Zheng J, Sheng Z-M, Peng X-Y and Zhang J 2005 Energetic electrons and protons generated from the interaction of ultrashort laser pulses with microdroplet plasmas *Phys. Plasmas* **12** 113105
- [34] Fraley G S, Linnebur E J, Mason R J and Morse R L 1974 Thermonuclear burn characteristics of compressed deuterium–tritium microspheres *Phys. Fluids* **17** 474–89
- [35] Nikifirov A F and Uvarov V B 1970 *Sov. Phys. Tech. Phys.* **15** 363
- [36] Ter-Avetisyan S, Schnurer M, Nickles P V, Smirnov M B, Sandner W, Andreev A, Platonov K, Psikal J and Tikhonchuk V 2008 Laser proton acceleration in a water spray target *Phys. Plasmas* **15** 083106
- [37] Sentoku Y, Cowan T E, Kemp A and Ruhl H 2003 High energy proton acceleration in interaction of short laser pulse with dense plasma target *Phys. Plasmas* **10** 2009
- [38] Lefebvre E and Bonnaud G Nonlinear electron heating in ultrahigh-intensity-laser–plasma interaction *Phys. Rev. E* **55** 1011
- [39] Andreev A A and Platonov K Yu 2000 Hard x-ray generation and particle production via the relativistic-intensity laser pulse interaction with a solid target *Laser Part. Beams* **18** 81
- [40] Andreev A A, Ceccotti T, Levy A, Platonov K and Martin Ph 2010 Divergence of fast ions generated by interaction of intense ultra-high contrast laser pulses with thin foils *New J. Phys.* **12** 045007
- [41] Zeil K, Kraft S D, Bock S, Bussmann M, Cowan T E, Kluge T, Metzkes J, Richter T, Sauerbrey R and Schramm U 2010 The scaling of proton energies in ultrashort pulse laser plasma acceleration *New J. Phys.* **12** 045015